Modeling the H$_2$O submillimeter emission in extragalactic sources⋆

E. González-Alfonso[1], J. Fischer[2], S. Aalto[3], and N. Falstad[3]

[1] Universidad de Alcalá, Departamento de Física y Matemáticas, Campus Universitario, 28871 Alcalá de Henares, Madrid, Spain
e-mail: eduardo.gonzalez@uah.es
[2] Naval Research Laboratory, Remote Sensing Division, 4555 Overlook Ave SW, Washington, DC 20375, USA
[3] Department of Earth and Space Sciences, Chalmers University of Technology, Onsala Space Observatory, 43992 Onsala, Sweden

ABSTRACT

Recent observational studies have shown that H$_2$O emission at (rest) submillimeter wavelengths is ubiquitous in infrared galaxies, both in the local and in the early Universe, suggestive of far-infrared pumping of H$_2$O by dust in warm regions. In this work, models are presented that show that (*i*) the highest-lying H$_2$O lines ($E_{upper} > 400$ K) are formed in very warm ($T_{dust} \gtrsim 90$ K) regions and require high H$_2$O columns ($N_{H_2O} \gtrsim 3 \times 10^{17}$ cm^{-2}), while lower lying lines can be efficiently excited with $T_{dust} \sim 45-75$ K and $N_{H_2O} \sim (0.5-2) \times 10^{17}$ cm^{-2}; (*ii*) significant collisional excitation of the lowest lying ($E_{upper} < 200$ K) levels, which enhances the overall $L_{H_2O}-L_{IR}$ ratios, is identified in sources where the ground-state para-H$_2$O $1_{11}-0_{00}$ line is detected in emission; (*iii*) the H$_2$O-to-infrared ($8-1000$ μm) luminosity ratio is expected to decrease with increasing T_{dust} for all lines with $E_{upper} \lesssim 300$ K, as has recently been reported in a sample of LIRGs, but increases with T_{dust} for the highest lying H$_2$O lines ($E_{upper} > 400$ K); (*iv*) we find theoretical upper limits for L_{H_2O}/L_{IR} in warm environments, owing to H$_2$O line saturation; (*v*) individual models are presented for two very different prototypical galaxies, the Seyfert 2 galaxy NGC 1068 and the nearest ultraluminous infrared galaxy Arp 220, showing that the excited submillimeter H$_2$O emission is dominated by far-infrared pumping in both cases; (*vi*) the $L_{H_2O}-L_{IR}$ correlation previously reported in observational studies indicates depletion or exhaustion time scales, $t_{dep} = \Sigma_{gas}/\Sigma_{SFR}$, of $\lesssim 12$ Myr for star-forming sources where lines up to $E_{upper} = 300$ K are detected, in agreement with the values previously found for (U)LIRGs from HCN millimeter emission. We conclude that the submillimeter H$_2$O line emission other than the para-H$_2$O $1_{11}-0_{00}$ transition is pumped primarily by far-infrared radiation, though some collisional pumping may contribute to the low-lying para-H$_2$O $2_{02}-1_{11}$ line, and that collisional pumping of the para-1_{11} and ortho-2_{12} levels enhances the radiative pumping of the higher lying levels.

Key words. line: formation – galaxies: ISM – infrared: galaxies – submillimeter: galaxies

1. Introduction

With its high dipolar moment, extremely rich spectrum, and high level spacing (in comparison to those of other molecules with low-lying transitions at millimeter wavelengths), H$_2$O couples very well to the radiation field in warm regions that emit strongly in the far-IR. In extragalactic sources, excited lines of H$_2$O at far-IR wavelengths ($\lambda < 200$ μm) were detected in absorption with the Infrared Space Telescope (ISO; Fischer et al. 1999; González-Alfonso et al. 2004, 2008), and with *Herschel*/PACS (Pilbratt et al. 2010; Poglitsch et al. 2010) in Mrk 231 (Fischer et al. 2010), Arp 220 and NGC 4418 (González-Alfonso et al. 2012, G-A12). Modeling and analysis have demonstrated the ability of H$_2$O to be efficiently excited through absorption of far-IR dust-emitted photons, thus providing a powerful method for studying the strength of the far-IR field in compact/warm regions that are not spatially resolved at far-IR wavelengths with current (or foreseen) technology.

Herschel/SPIRE (Griffin et al. 2010) has enabled the observation of H$_2$O at submillimeter (hereafter submm, $\lambda > 200$ μm) wavelengths in local sources, where the excited (i.e., non-ground-state) lines are invariably seen in emission. In Mrk 231, lines with E_{upper} up to 640 K were detected (van der Werf et al. 2010; González-Alfonso et al. 2010, hereafter G-A10), with strengths comparable to the CO lines. The H$_2$O lines have

been also detected in other local sources (Rangwala et al. 2011; Pereira-Santaella et al. 2013), including the Seyfert 2 galaxy NGC 1068 (Spinoglio et al. 2012, S12). Furthermore, submm lines of H$_2$O have been detected in a dozen of high-z sources (Impellizzeri et al. 2008; Omont et al. 2011; Lis et al. 2011; van der Werf et al. 2011; Bradford et al. 2011; Combes et al. 2012; Lupu et al. 2012; Bothwell et al. 2013), even in a $z = 6.34$ galaxy (Riechers et al. 2013). Recently, a striking correlation has been found between the submm H$_2$O luminosity (L_{H_2O}), taken from the $2_{02}-1_{11}$ and $2_{11}-2_{02}$ lines, and the IR luminosity (L_{IR}), including both local and high-z ULIRGs (Omont et al. 2013, hereafter O13). Using SPIRE spectroscopy of local IR-bright galaxies and published data from high-z sources, the linear correlations between L_{H_2O} and L_{IR} for five of the strongest lines, extending over more than three orders of magnitude in IR luminosity, has recently been confirmed (Yang et al. 2013, hereafter Y13). There are hints of an increase in L_{H_2O} that is slightly faster than linear with L_{IR} in some lines ($2_{11}-2_{02}$ and $2_{20}-2_{11}$) and in high-z ULIRGs (O13). HCN is another key species that also shows a tight correlation with the IR luminosity, even though the excitation of the 1−0 transition is dominated by collisions with dense H$_2$ (Gao & Solomon 2004a,b).

The increasing wealth of observations of H$_2$O at submm wavelengths in both local and high-z sources and the correlations discovered between L_{H_2O} and L_{IR} require a more extended analysis in parameter space than the one given in G-A10 for Mrk 231. In this work, models are presented to constrain the

---

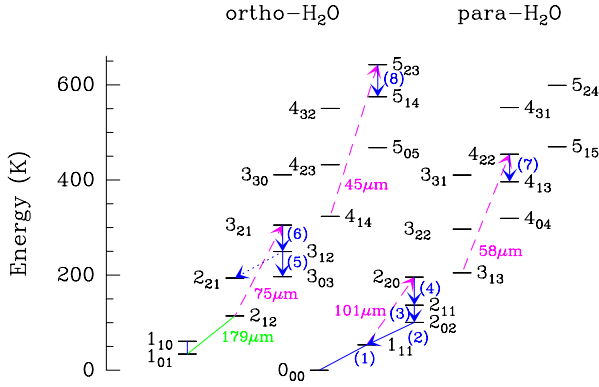⋆ Appendix A is available in electronic form at
http://www.aanda.org

Fig. 1. Energy level diagram of H_2O, showing the relevant H_2O lines at submillimeter wavelengths with blue arrows, and the far-IR H_2O pumping (absorption) lines with dashed-magenta arrows. The lines are numbered as listed in Table 1. The o-H_2O $3_{12}-2_{21}$ transition is not considered due to blending with CO (10-9) (G-A10), and the far-IR $2_{12}-1_{01}$ transition at 179.5 μm discussed in the text is also indicated in green for completeness.

physical and chemical conditions in the submm H_2O emitting regions in warm (U)LIRGs and to propose a general framework for interpreting the H_2O submm emission in extragalactic sources.

2. Excitation overview

At submm wavelengths, H_2O responds to far-IR excitation by emitting photons through a cascade proccess. This is illustrated in Fig. 1, where four far-IR pumping lines (at 101, 75, 58, and 45 μm) account for the radiative excitation of the submm lines (G-A10). The line parameters are listed in Table 1, where we use the numerals 1−8 to denote the submm lines. Lines 2−4, 5−6, 7, and 8 are pumped through the 101[1], 75, 58, and 45 μm far-IR transitions, respectively.

The ground-state line 1 has no analog pumping mechanism, so that the upper 1_{11} level can only be excited through absorption of a photon in the same transition (at 269 μm) or through a collisional event. In the absence of significant collisional excitation, and if approximate spherical symmetry holds, line 1 will give negligible absorption or emission above the continuum (regardless of line opacity) if the continuum opacity at 269 μm is low or will be detected in absorption for significant 269 μm continuum opacities[2]. This is supported by the SPIRE spectrum of Arp 220, in which line 1 is observed in absorption (Rangwala et al. 2011) and high submm continuum opacities are inferred (González-Alfonso et al. 2004; Downes & Eckart 2007; Sakamoto et al. 2008). Collisional excitation and thus high densities and gas temperatures are then expected in sources where line 1 is detected in emission (10 sources among 176, Y13), as in NGC 1068 (S12; see also Appendix A). Line 1 can then be collisionally excited in regions where the other lines do not emit owing to weak far-IR continuum; this effect has recently been observed in the intergalactic filament in the Stephan's Quintet (Appleton et al. 2013).

If collisional excitation of the 1_{11} and 2_{12} levels dominates over absorption of dust photons at 269 and 179 μm (i.e., in very optically thin and/or high density sources), the submm H_2O lines

[1] This line lies within the PACS 100 μm gap, but was detected in Arp 220 and Mrk 231 with *ISO* (González-Alfonso et al. 2004, 2008).
[2] This is analogous to the behavior of the OH 119 μm doublet, see González-Alfonso et al. (2014).

Table 1. H_2O transitions at $\lambda > 200\,\mu$m considered in this work.

N	Transition		$E_{\rm upper}$ (K)	$\lambda_{\rm rest}$ (μm)	$A_{\rm ul}$ (s^{-1})
1	H_2O	$1_{11}-0_{00}$	53	269.27	0.018
2	H_2O	$2_{02}-1_{11}$	101	303.46	0.006
3	H_2O	$2_{11}-2_{02}$	137	398.64	0.007
4	H_2O	$2_{20}-2_{11}$	196	243.97	0.019
5	H_2O	$3_{12}-3_{03}$	249	273.19	0.016
6	H_2O	$3_{21}-3_{12}$	305	257.79	0.023
7	H_2O	$4_{22}-4_{13}$	454	248.25	0.028
8	H_2O	$5_{23}-5_{14}$	642	212.53	0.043

Table 2. Model parameters.

Parameter	Explored range	Best fit to HII+mild AGN[a]
$T_{\rm dust}$ (K)	35−115	45−75
τ_{100}	0.02−12	0.05−0.2
$N_{\rm H_2O}/\Delta V$ (cm^{-2}/(km s^{-1}))	$3 \times 10^{14}-10^{16}$	$(0.5-2) \times 10^{15}$
ΔV^c (km s^{-1})	100	[b]
$n_{\rm H_2}$ (cm^{-3})	$2 \times 10^4-3 \times 10^5$	$\lesssim 3 \times 10^5$
$T_{\rm gas}$ (K)	100−200	[b]

Notes. [a] Best fit values for HII+mild AGN sources (optically classified star-formation dominated galaxies with possible mild AGN contribution, see Y13 and Sect. 5) for which lines 2−6 are detected, but lines 7−8 are undetected. [b] Parameter not well constrained. [c] FWHM velocity dispersion of the dominant H_2O emitting structures, in our models equal to $1.67V_{\rm turb}$.

2−6 will be boosted because these 1_{11} and 2_{12} levels are the *base levels* from which the 101 and 75 μm radiative pumping cycles operate (Fig. 1). In addition, in regions of low continuum opacities but warm gas, collisional excitation of the para-H_2O level 2_{02} from the ground 0_{00} state can significantly enhance the emission of line 2. Therefore, the H_2O submm emission depends in general on both the far-IR radiation density in the emitting region and the possible collisional excitation of the low-lying levels (1_{11}, 2_{12}, and 2_{02}). Lines 7−8 require strong far-IR radiation density not only at 58−45 μm, but also at longer wavelengths, together with high H_2O column densities ($N_{\rm H_2O}$) in order to significantly populate the lower backbone 3_{13} and 4_{14} levels.

3. Description of the models

The basic models for H_2O were described in G-A10 (see also references therein). Summarizing, we assume a simple spherically symmetric source with uniform physical properties ($T_{\rm dust}$, $T_{\rm gas}$, gas and dust densities, H_2O abundance), where gas and dust are assumed to be mixed. We only consider the far-IR radiation field generated within the modeled source, ignoring the effect of external fields (except for NGC 1068, Appendix A). The source is divided into a set of spherical shells where the statistical equilibrium level populations are calculated. The models are non-local, including line and continuum opacity effects. We assume an H_2O ortho-to-para ratio of 3. Line broadening is simulated by including a microturbulent velocity ($V_{\rm turb}$), for which the FWHM velocity dispersion is $\Delta V = 1.67V_{\rm turb}$. No systemic motions are included.
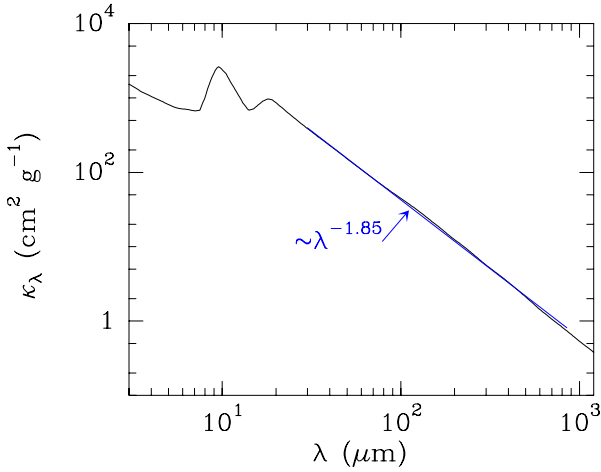
Fig. 2. Adopted mass absorption coefficient of dust as a function of wavelength. The dust emission is simulated by using a mixture of silicate and amorphous carbon grains with optical constants from Draine (1985) and Preibisch et al. (1993). As shown by the fitted blue line, the emissivity index from the far-IR to millimeter wavelengths is $\beta = 1.85$.

3.1. Mass absorption coefficient of dust

The black curve in Fig. 2 shows the dust mass opacity coefficient used in the current and our past models (González-Alfonso et al. 2008, 2010, 2012, 2013, 2014). Our values at 125 and 850 μm are $\kappa_{125} = 30$ cm^2 g^{-1} and $\kappa_{850} = 0.7$ cm^2 g^{-1}, in good agreement with those derived by Dunne et al. (2003). Adopting a gas-to-dust ratio of $X = 100$ by mass, and using $\kappa_{100} = 44.5$ cm^2 g^{-1}, the column density of H nuclei is

$$N_{\rm H} = \frac{X\,\tau_{100}}{m_{\rm H}\,\kappa_{100}} = 1.3 \times 10^{24}\,\tau_{100}\ {\rm cm}^{-2}, \qquad (1)$$

where τ_{100} is the continuum optical depth at 100 μm.

For this adopted dust composition, the fit across the far-IR to submm (blue line in Fig. 2) indicates an emissivity index of $\beta = 1.85$, slightly steeper than the $\beta = 1.5-1.6$ values favored by Kóvacs et al. (2010) and Casey (2012). The H$_2$O excitation is sensitive to the dust emission over a range of wavelengths (from 45 to 270 μm), but we find that our results on $L_{\rm H_2O}/L_{\rm IR}$ are insensitive to β for β values above 1.5 (Sect. 4.3.3).

3.2. Model parameters

As listed in Table 2, the model parameters we have chosen to characterize the physical conditions in the emitting regions are $T_{\rm dust}$, the continuum optical depth at 100 μm along a radial path (τ_{100}), the corresponding H$_2$O column density per unit of velocity interval ($N_{\rm H_2O}/\Delta V$), the velocity dispersion ΔV, $T_{\rm gas}$, and the H$_2$ density ($n_{\rm H_2}$). Fiducial numbers for some of these parameters are $\tau_{100} = 0.1$, $\Delta V = 100$ km s^{-1}, $T_{\rm gas} = 150$ K, and $n_{\rm H_2} = 3 \times 10^5$ cm^{-3}. Collisional rates with H$_2$ were taken from Dubernet et al. (2009) and Daniel et al. (2011). Our relevant results are the line-flux ratios (F_i/F_j) and the luminosity ratios[3] $L_{\rm H_2O}/L_{\rm IR}$. We also explore models where collisions are ignored, appropriate for low-density regions ($n_{\rm H_2} \lesssim 10^4$ cm^{-3}), for which F_i/F_j only depend on $T_{\rm dust}$, τ_{100}, and $N_{\rm H_2O}/\Delta V$, while $L_{\rm H_2O}/L_{\rm IR}$ depends in addition on ΔV.

---

[3] We denote $L_{\rm H_2O}$ as the H$_2$O luminosity *of a given generic* H$_2$O submm line, while L_i is the luminosity of the H$_2$O line *i* (numbering in Table 1). The H$_2$O line fluxes F_i are given in Jy km s^{-1}. $L_{\rm IR}$ is the 8−1000 μm luminosity.

Depending on the values of the above parameters, our models can be interpreted in terms of a single source or are better applied to each of an ensemble of clouds within a clumpy distribution. The radius of the modeled source is

$$R = N_{\rm H}/n_{\rm H} = 0.21 \times \left(\frac{\tau_{100}}{0.1}\right) \times \left(\frac{10^5\ {\rm cm}^{-3}}{n_{\rm H_2}}\right)\ {\rm pc}, \qquad (2)$$

where Eq. (1) has been applied. The corresponding IR luminosity can be written as $L_{\rm IR} = 4\pi R^2 \sigma T_{\rm dust}^4\,\gamma$, where $\gamma(T_{\rm dust}, \tau_{100}) \leq 1$ accounts for the departure from a blackbody emission due to finite optical depths, ranging from $\gamma = 0.2$ for $T_{\rm dust} = 50$ K and $\tau_{100} = 0.1$ to $\gamma = 0.9$ for $T_{\rm dust} = 95$ K and $\tau_{100} = 1$. In physical units,

$$L_{\rm IR} = 1.4 \times 10^5 \times \left(\frac{\tau_{100}}{0.1}\right)^2 \times \left(\frac{10^5\ {\rm cm}^{-3}}{n_{\rm H_2}}\right)^2 \times \left(\frac{T_{\rm dust}}{55\ {\rm K}}\right)^4 \times \left(\frac{\gamma}{0.2}\right) \quad (3)$$

in $L_\odot$, indicating that a model with $\tau_{100} \sim 0.1$ and moderate $T_{\rm dust}$ should be considered as one of an ensemble of clumps to account for the typically observed IR luminosities of $\gtrsim 10^{11}\ L_\odot$ (Y13). For very warm ($T_{\rm dust} \sim 90$ K) and optically thick ($\tau_{100} \sim 1$) sources with low average densities ($n_{\rm H_2} = 3 \times 10^3$ cm^{-3}), Eq. (3) gives $L_{\rm IR} \sim 5 \times 10^{11}\ L_\odot$ and the model can be applied to a significant fraction of the circumnuclear region of galaxies where the clouds may have partially lost their individuality (Downes & Solomon 1998).

The velocity dispersion ΔV in our models can be related to the velocity gradient used in escape probability methods as dV/d$r \sim \Delta V/(2R)$, and using Eq. (2)

$$\mathrm{d}V/\mathrm{d}r \sim 238 \times \left(\frac{\Delta V}{100\ {\rm km\,s}^{-1}}\right) \times \left(\frac{0.1}{\tau_{100}}\right) \times \left(\frac{n_{\rm H_2}}{10^5\ {\rm cm}^{-3}}\right)\ {\rm km\,s}^{-1}\,{\rm pc}^{-1}. \qquad (4)$$

Defining $K_{\rm vir}$ as the ratio of the velocity gradient relative to that expected in gravitational virial equilibrium, $K_{\rm vir} = ({\rm d}V/{\rm d}r)/({\rm d}V/{\rm d}r)_{\rm vir}$, and using $({\rm d}V/{\rm d}r)_{\rm vir} \sim 10 \times (n_{\rm H_2}/10^5\ {\rm cm}^{-3})^{1/2}$ km s^{-1} pc^{-1} (Bryant & Scoville 1996; Goldsmith 2001; Papadopoulos et al. 2007; Hailey-Dunsheath et al. 2012), we obtain

$$K_{\rm vir} \sim 23.8 \times \left(\frac{\Delta V}{100\ {\rm km\,s}^{-1}}\right) \times \left(\frac{0.1}{\tau_{100}}\right) \times \left(\frac{n_{\rm H_2}}{10^5\ {\rm cm}^{-3}}\right)^{1/2}. \qquad (5)$$

Values of $K_{\rm vir}$ significantly above 1 and up to ~ 20, indicating non-virialized phases, have been inferred in luminous IR galaxies from both low- and high-J CO lines (e.g., Papadopoulos & Seaquist 1999; Papadopoulos et al. 2007; Hailey-Dunsheath et al. 2012). For clarity, the velocity dispersion is rewritten in terms of $K_{\rm vir}$ as

$$\Delta V = 42 \times \left(\frac{K_{\rm vir}}{10}\right) \times \left(\frac{\tau_{100}}{0.1}\right) \times \left(\frac{10^5\ {\rm cm}^{-3}}{n_{\rm H_2}}\right)^{1/2}\ {\rm km\,s}^{-1}, \qquad (6)$$

which shows that, for compact and dense clumps ($\tau_{100} = 0.1$, $n_{\rm H_2} = 3 \times 10^5$ cm^{-3}), $\Delta V \sim 25 \times (K_{\rm vir}/10)$ km s^{-1} and the typical observed linewidths (~ 300 km s^{-1}) are caused by the galaxy rotation pattern and velocity dispersion of clumps. In contrast, for optically thick sources with low densities ($\tau_{100} = 1$, $n_{\rm H_2} \lesssim 10^4$ cm^{-3}), $\Delta V \gtrsim 130$ km s^{-1} is required for $K_{\rm vir} \gtrsim 1$.

Instead of calculating ΔV for each model according to Eq. (6), which would involve a "universal" $K_{\rm vir}$ independent of

the source characteristics[4], we have used $\Delta V = 100\ \mathrm{km\,s^{-1}}$ for comparison purposes between models (in Sect. 4.3.5 we also consider models with constant K_{vir}). Nevertheless, results can be easily rescaled to any other value of ΔV as follows. For given T_{dust} and τ_{100}, the relative level populations, the line opacities, and thus the H_2O line-flux ratios (F_i/F_j) depend on $N_{H_2O}/\Delta V$, while the luminosity ratios L_{H_2O}/L_{IR} are proportional to ΔV. Therefore, for any ΔV, identical results for F_i/F_j are obtained with the substitution

$$N_{H_2O} \rightarrow N_{H_2O} \times \left(\frac{\Delta V}{100\ \mathrm{km\,s^{-1}}}\right), \tag{7}$$

while L_{H_2O}/L_{IR} should be scaled as

$$\frac{L_{H_2O}}{L_{\mathrm{IR}}} \rightarrow \frac{L_{H_2O}}{L_{\mathrm{IR}}} \times \left(\frac{\Delta V}{100\ \mathrm{km\,s^{-1}}}\right). \tag{8}$$

Both the line-flux ratios (F_i/F_j) and the luminosity ratios L_{H_2O}/L_{IR} are independent of the number of clumps (N_{cl}) if the model parameters (T_{dust}, τ_{100}, T_{gas}, n_{H_2}, $N_{H_2O}/\Delta V$, and ΔV) remain the same for the cloud average. With the effective source radius defined as $R_{\mathrm{eff}} = N_{\mathrm{cl}}^{1/2} R$, both the line and continuum luminosities scale as $\propto R_{\mathrm{eff}}^2$. Therefore, if the effective source size is changed and all other parameters are kept constant, a linear correlation between each L_{H_2O} and L_{IR} is naturally generated, regardless of the excitation mechanism of H_2O. (For reference, however, all absolute luminosities below are given for $R_{\mathrm{eff}} = 100$ pc.) The question, then, is what range of dust and gas parameters characterizes the sources for which the observed nearly linear correlations in lines 2−6 (O13, Y13) are observed. The detection rates of lines 1, 7, and 8 are relatively low, but the same trend is observed in the few sources where they are detected (Y13).

In the following sections, the general results of our models are presented, while specific fits to two extreme sources, Arp 220 and NGC 1068, are discussed in Appendix A.

4. Model results

4.1. General results

In Fig. 3, model results are shown in which T_{dust} is varied from 35 to 115 K, $N_{H_2O}/\Delta V$ from 5×10^{14} to $5 \times 10^{15}\ \mathrm{cm^{-2}/(km\,s^{-1})}$, τ_{100} from 0.1 to 1.0, and where collisional excitation with $n_{H_2} = 3 \times 10^5\ \mathrm{cm^{-3}}$ and $T_{\mathrm{gas}} = 150$ K is excluded (a−c) or included (d−f). Panels a1−f1 (top) show the expected SLED normalized to line 2, and panels a2-f2 (bottom) plot the corresponding $L_{H_2O}/L_{\mathrm{IR}} \times (100\ \mathrm{km\,s^{-1}}/\Delta V)$ ratios as a function of T_{dust} and L_{IR} (for $R_{\mathrm{eff}} = 100$ pc; all points would move horizontally for different R_{eff}). The effect of collisional excitation is also illustrated in Fig. 4, where the H_2O submm fluxes of lines 2−6 relative to those obtained ignoring collisional excitation are plotted as a function of n_{H_2} for $T_{\mathrm{gas}} = 150$ K.

The first conclusion that we infer from Figs. 3a1-f1 is that the relative fluxes of lines 5−6 generally increase with increasing T_{dust}. These lines are pumped through the H_2O transition at $\lambda \sim 75\ \mu\mathrm{m}$ (Fig. 1), thus requiring warmer dust than lines 2−4,

which are pumped through absorption of 100 μm photons. The SLEDs obtained with $T_{\mathrm{dust}} < 45$ K yield F_4 significantly above F_6, and are thus unlike those observed in most (U)LIRGs (Y13). The two peaks in the H_2O SLED (in lines 2 and 6) generally found in (U)LIRGs (Y13) indicate that the submm H_2O emission essentially samples regions with $T_{\mathrm{dust}} \gtrsim 45$ K. Significant collisional excitation enhances line 4 relative to line 6 (Figs. 3d1−f1), thus aggravating the discrepancy between the $T_{\mathrm{dust}} < 45$ K models and the observations.

Lines 7−8 provide stringent constraints on T_{dust}, τ_{100}, and $N_{H_2O}/\Delta V$. Since line 6 is still easily excited even with moderately warm $T_{\mathrm{dust}} \sim 55$ K, the 8/6 and 7/6 ratios are good indicators of whether very warm dust (>80 K) is exciting H_2O. Sources where lines 7−8 are detected (e.g., Mrk 231, Arp 220, and APM 08279) can be considered "very warm" on these grounds, with $N_{H_2O}/\Delta V \gtrsim 3 \times 10^{15}\ \mathrm{cm^{-2}/(km\,s^{-1})}$. Sources where lines 7−8 are not detected to a significant level, but where the SLED still shows a second peak in line 6, are considered "warm", i.e. with T_{dust} varying between ~45 and 80 K, and $N_{H_2O}/\Delta V \sim (5-20) \times 10^{14}\ \mathrm{cm^{-2}/(km\,s^{-1})}$.

Sources in which lines 2−6 are not detected to a significant level, that do not show a second peak in line 6, or for which the H_2O luminosities are well below the observed $L_{H_2O}-L_{\mathrm{IR}}$ correlation are considered "cold". These sources are characterized by very optically thin and extended continuum emission, and/or with low N_{H_2O} (these properties likely go together). Such sources include starbursts like M82 (Y13), where the continuum is generated in PDRs and are physically very different from the properties of "very warm" sources like Mrk 231 (G-A10).

In the models that neglect collisional excitation (a1−c1), line 1 is predicted to be in absorption, transitioning to emission in warm/dense regions where it is collisionally excited (d1−f1), as previously argued. Its strength will also depend on the continuum opacity, which should be low enough to allow the line to emit above the continuum. Direct collisional excitation from the ground state in regions with warm gas but low τ_{100} efficiently populates level 2_{02}, so that the 2/3, 2/4, 2/5, and 2/6 ratios strongly increase with increasing n_{H_2} (Fig. 4a). As advanced in Sect. 2, collisional excitation also boosts all other submm lines for moderate T_{dust} owing to efficient pumping of the base levels 2_{12} and 1_{11}; radiative trapping of photons emitted in the ground-state transitions increases the chance of absorption of continuum photons in the 101 and 75 μm transitions. Nevertheless, collisional excitation is negligible for high τ_{100} and high T_{dust} (Fig. 4b).

4.2. Predicted line ratios

In sources where lines 7 and 8 are not detected, the 6/4 flux ratio is the most direct indication of the hardness of the far-IR radiation field seen by the H_2O gas responsible for the observed emission. Since line 4 is pumped through absorption of 101 μm photons and line 6 by 75 μm photons (Fig. 1), one may expect a correlation between the 6/4 ratio and the 75-to-100 μm far-IR color, f_{75}/f_{100}. As shown in Fig. 5a, our models indeed show a steep increase in the 6/4 ratio with T_{dust} for fixed τ_{100} and N_{H_2O}. The averaged observed 6/4 ratio of $\approx 1.45-1.7$ in strong-AGN and HII+mild-AGN sources (Y13) indicates, assuming an optically thin continuum (Fig. 5a), $T_{\mathrm{dust}} \approx 55-75$ K and $f_{75}/f_{100} = 1.5-1.8$. For the case of high τ_{100} and $N_{H_2O}/\Delta V$, the averaged 6/4 ratio is consistent with lower T_{dust} and $f_{75}/f_{100} = 1-1.2$.

---

[4] We may expect $K_{\mathrm{vir}} > 1$ for clouds in a clumpy distribution due to the gravitational potential of the galaxy and external pressure (Papadopoulos & Seaquist 1999), but $K_{\mathrm{vir}} \sim 1$ may be more appropriate for sources where the clouds have coalesced and the resulting (modeled) structure can be considered more isolated. However, $K_{\mathrm{vir}} > 1$ in case of prominent outflows.
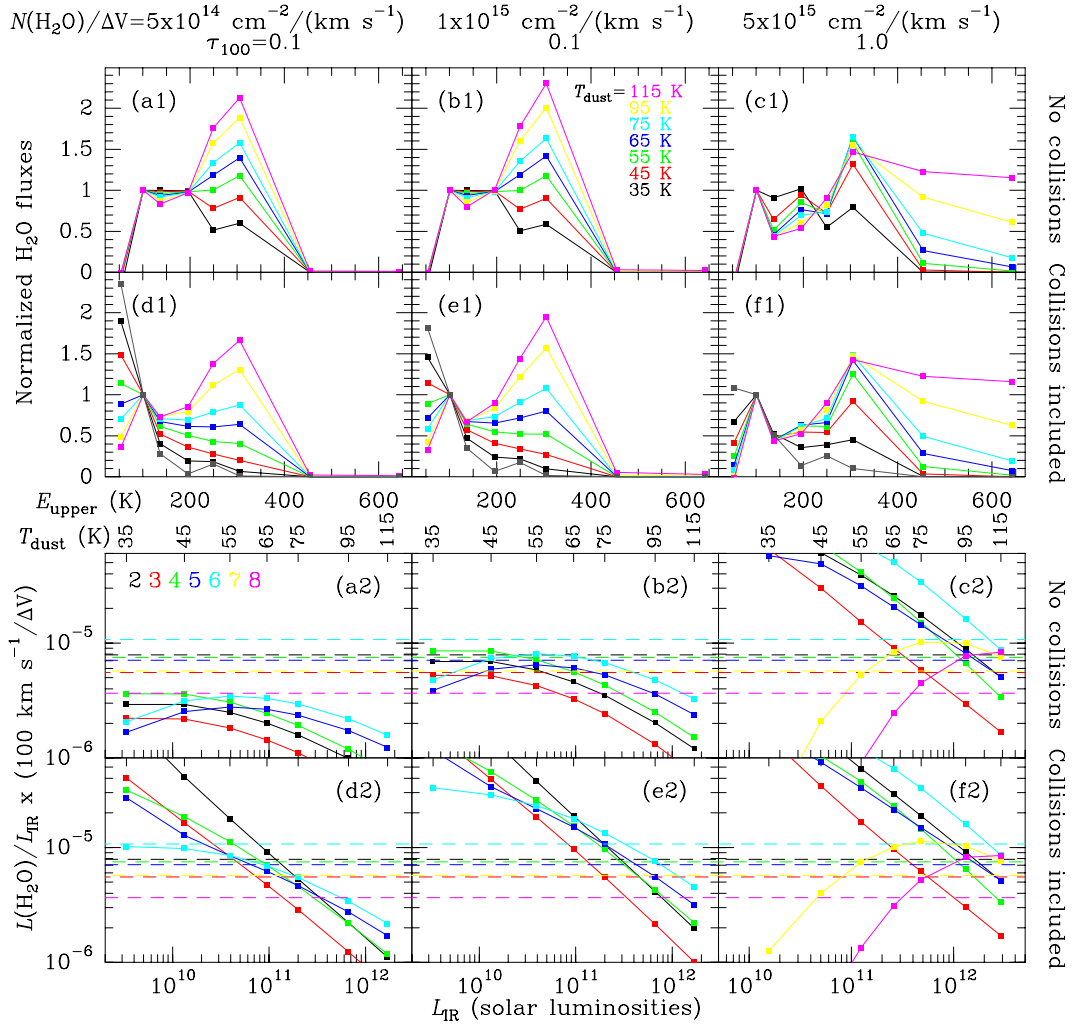
Fig. 3. Relevant model results for the normalized H$_2$O SLED (**a1**)−**f1**)), and for the L_{H_2O}/L_{IR} ratios (for $\Delta V = 100$ km s^{-1}) as a function of T_{dust} and L_{IR} (assuming a source of $R_{eff} = 100$ pc, **a2**)−**f2**)). In panels **a1**)–**f1**), model results for lines 1 to 8 (Table 1) are shown from left to right. Values for $N_{H_2O}/\Delta V$ and τ_{100} are indicated at the top of the figure. The different colors in panels **a1**)–**f1**) indicate different T_{dust}, as labeled in **b1**), while they indicate different lines in panels **a2**)–**f2**) (labeled in **a2**), see Table 1. Models with collisional excitation ignored (**a**)−**c**)), and with collisions included for $n_{H_2} = 3 \times 10^5$ cm^{-3} and $T_{gas} = 150$ K (**d**)−**f**)) are shown. The gray lines/symbols in panels **d1**)−**f1**) show model results that ignore radiative pumping (i.e., only collisional excitation). Collisional excitation has the overall effect of enhancing the low-lying lines (1 and 2) relative to the others and of increasing the L_{H_2O}/L_{IR} ratios of all lines (see text). The dashed lines in panels **a2**)−**f2**) indicate the average L_{H_2O}/L_{IR} ratios reported by Y13. When compared with observations, the modeled L_{IR} values should be considered a fraction of the observed IR luminosities, because single temperature dust models are unable to reproduce the observed SEDs (Sect. 4.3.1); the H$_2$O submm emission traces warm regions of luminous IR galaxies (see text).

In general, the 6/4 ratio indicates $T_{dust} \approx 45–80$ K[5]. Similarly, the 6/2 ratio is also sensitive to T_{dust}, as shown in Fig. 5b. The observed averaged 6/2 ratio of $\approx 1–1.2$ is compatible with T_{dust} somewhat lower than estimated from the 6/4 ratio. This is attributable to the effects of collisional excitation of the 2_{02} level (thus enhancing line 2 over line 6, see Fig. 4a and magenta symbols in Fig. 5b), or to the contribution to line 2 by an extended, low T_{dust} component.

There is, however, no observed correlation between the 6/4 ratio and f_{60}/f_{100} (Y13), which should still show a correlation (though maybe less pronounced) than the expected correlation with f_{75}/f_{100}. As we argue in Sect. 4.3, this lack of correlation suggests that the observed far-IR f_{60}/f_{100} colors, and in particular the observed f_{100} fluxes, are not dominated by the warm component responsible for the H$_2$O emission. Indeed, current models for the continuum emission in (U)LIRGs indicate that the flux density at 100 μm is dominated by relatively cold dust components ($T_{dust} \sim 30$ K) (e.g. Dunne et al. 2003; Kóvacs et al. 2010; Casey 2012). The observed H$_2$O emission thus arises in warm regions whose continuum is hidden within the observed far-IR emission, but may dominate the observed SED at $\lambda \lesssim 50$ μm (e.g., Casey 2012, see also Sect. 4.3.1).

The H$_2$O lines 5 and 6 are both pumped through the 75 μm transition. Assuming that the lines are optically thin, statistical equilibrium of the level populations implies that every de-excitation in line 6 will be followed by a de-excitation in either
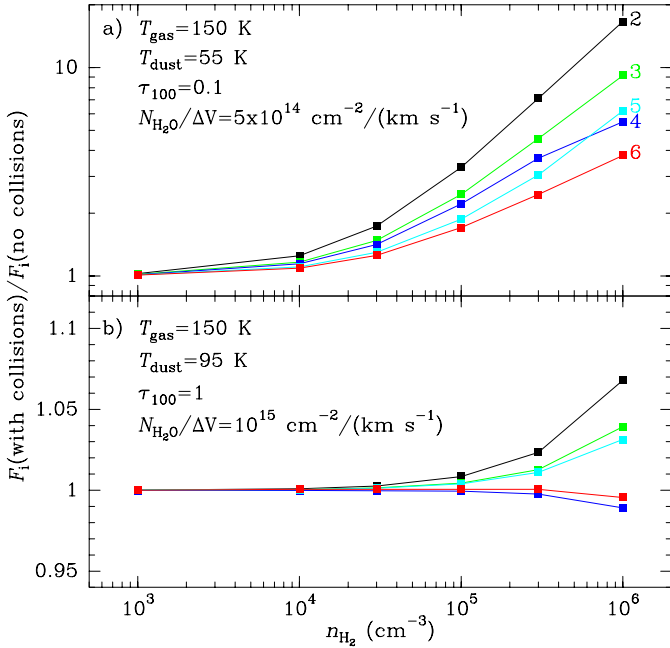
---

[5] Such high T_{dust} can be explained in the optically thin case as follows: first, the para-1_{11} level is more easily populated through radiation than the ortho-2_{12} level, because the B_{lu}/A_{ul} ratio for the $1_{11}–0_{00}$ transition is a factor 6 higher than for the $2_{12}–1_{01}$ one (B_{lu} and A_{ul} are the Einstein coefficients for photo absorption and spontaneous emission). Second, the B_{lu} coefficient of the para-$2_{20}–1_{11}$ pumping transition is a factor of ≈ 2.3 higher than that of the ortho-$3_{21}–2_{12}$ pumping transition. Taking into account an ortho-to-para ratio of 3, a 6/4 ratio of 1 is obtained for $J_{179}J_{75}/(J_{269}J_{101}) \approx 4.5$ (J_λ is the mean specific intensity at wavelength λ), which requires $T_{dust} \approx 45$ K.

Fig. 4. Effect of collisional excitation on the H$_2$O fluxes of the submm lines 2−6 as a function of n_{H_2}. The ordinates show the calculated line fluxes relative to the model that ignores collisional excitation. T_{gas} = 150 K is adopted in all models. **a)** In the case of moderate T_{dust} and low τ_{100}, collisional excitation has a strong impact on the H$_2$O fluxes at n_{H_2} of a few × 10^4 cm^{-3}, especially on line 2. **b)** Collisional excitation is negligible for high τ_{100} and very warm T_{dust} (note the difference in ordinate scales in **a)** and **b)**).

line 5 or in the $3_{12} - 2_{21}$ transition (dotted arrow in Fig. 1), with relative probablities determined by the A-Einstein coefficients. In these optically thin conditions, we expect a 6/5 line flux ratio of F_6/F_5 = 1.16 (Fig. 6). This is a lower limit, because in case of high $N_{H_2O}/\Delta V$ and/or high T_{dust} and τ_{100}, absorption of line 5 emitted photons that can eventually be reemitted through the $3_{12} - 2_{21}$ transition, or absorption of continuum photons in the H$_2$O $4_{23} - 3_{12}$ transition, will decrease the strength of line 5 relative to line 6.

Although with significant dispersion, overall data for HII+mild AGN sources indicate $F_6/F_5 \sim 1.2$ (Y13)[6], consistent with the optically thin limit; examples of this galaxy population are NGC 1068 and NGC 6240 (Spinoglio et al. 2012; Meijerink et al. 2013). There are, however, sources like Arp 220 and Mrk 231 with $F_6/F_5 \approx 1.6$, favoring warm dust (>55 K) and substantial columns of H$_2$O and dust. This indicates that sources in both the optically thin and optically thick regimes are H$_2$O emitters.

In optically thin conditions and with moderate T_{dust}, lines 2−4, together with the pumping $2_{20} - 1_{11}$ 101 μm transition, form a closed loop (Fig. 1) where statistical equilibrium of the level populations implies equal fluxes for the three submm lines (Figs. 3a1−c1). The rise in T_{dust} and τ_{100}, however, increases the chance of line absorption in the strong $3_{22} - 2_{11}$ transition at 90 μm, thus decreasing the flux of line 3 relative to both line 2 and 4. Consequently, the F_2/F_3 ratio is expected to increase from ≈1 (for low τ_{100}) to ≈2 (for $\tau_{100} \sim 1$ and $N_{H_2O}/\Delta V \gtrsim 10^{17}$ cm^{-2}/(km s^{-1})), consistent with the relatively

---

6 We infer this value from the $(L_{H_2O}/L_{IR})_2/(L_{H_2O}/L_{IR})_i$ ratios listed in Table 2 by Y13, though $F_6/F_5 \sim 1.4$ as derived directly from $(L_{H_2O}/L_{IR})_5/(L_{H_2O}/L_{IR})_6$, indicating that the averaged F_6/F_5 depends on the details (weights) of the average computation.
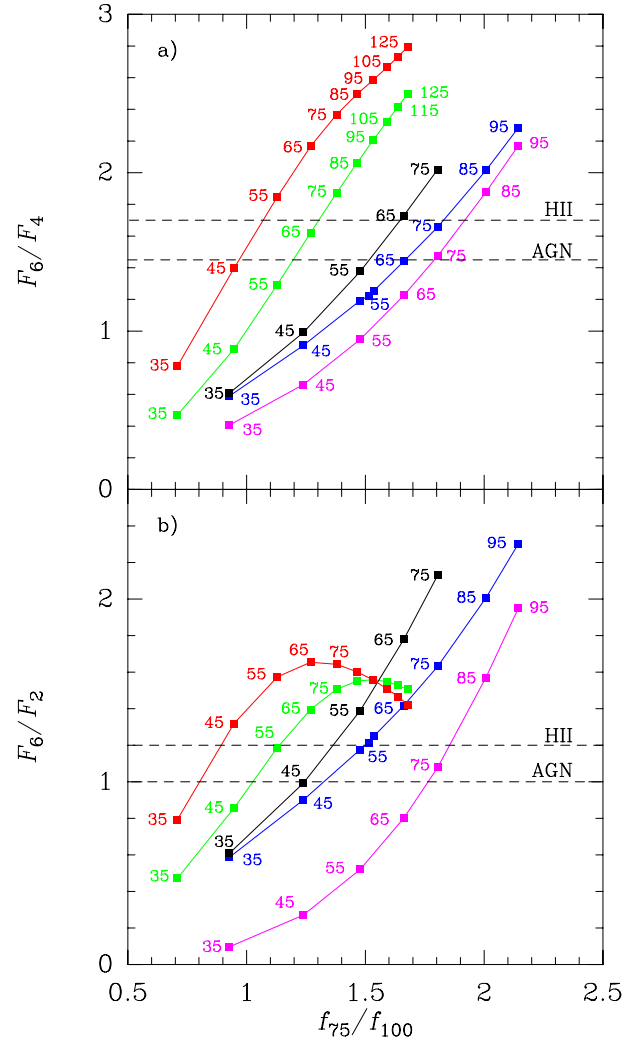
Fig. 5. a) F_6/F_4 (oH$_2$O $3_{21} - 3_{12}$-to-pH$_2$O $2_{20} - 2_{11}$) and **b)** F_6/F_2 (oH$_2$O $3_{21} - 3_{12}$-to-pH$_2$O $2_{02} - 1_{11}$) line flux ratios as a function of the 75-to-100 μm far-IR color. Blue symbols: $N_{H_2O}/\Delta V = 10^{15}$ cm^{-2}/(km s^{-1}) and $\tau_{100} \leq 0.1$; black: $N_{H_2O}/\Delta V = 5 \times 10^{15}$ cm^{-2}/(km s^{-1}) and $\tau_{100} \leq$ 0.1; red: $N_{H_2O}/\Delta V = 5 \times 10^{15}$ cm^{-2}/(km s^{-1}) and $\tau_{100} = 1.0$; green: $N_{H_2O}/\Delta V = 10^{15}$ cm^{-2}/(km s^{-1}) and $\tau_{100} = 1.0$; magenta: same as blue symbols but with collisional excitation included with $T_{gas} = 150$ K and $n_{H_2} = 3 \times 10^5$ cm^{-3}. The small numbers close to the symbols indicate the value of T_{dust}. The observed averaged ratios for strong-AGN and HII+mild-AGN sources (Y13) are indicated with dashed horizontal lines, and indicate that the regions probed by the H$_2$O submm emission are characterized by warm dust ($T_{dust} \gtrsim 45$ K).

high values found in the warm Mrk 231 and APM 08279 (Y13). If collisional excitation is important (Figs. 3d−f), F_2/F_3 is also expected to increase because collisions mainly boost the lower lying line 2 (Fig. 4a).

One interesting caveat is, however, the behavior of the 4/3 ratio, because increasing T_{dust} and/or N_{H_2O} is predicted to increase F_2/F_3 but maintains $F_4/F_3 > 1$ (Figs. 3a1−c1). In Mrk 231, the high F_2/F_3 ratio and mostly the detection of lines 7−8 indicate very warm dust (G-A10), but the relatively low $F_4/F_3 \lesssim 1$ observed in the source does not match this simple scheme. The problem is exacerbated with the 6/2 ratio, which is also expected to increase with increasing T_{dust} and τ_{100} to ≈1.5 (Fig. 5), but Mrk 231 shows $F_6/F_2 \approx 1$. Nevertheless, the problem can be solved if source structure is invoked. A composite model where a very warm component accounts for the high-lying lines and a
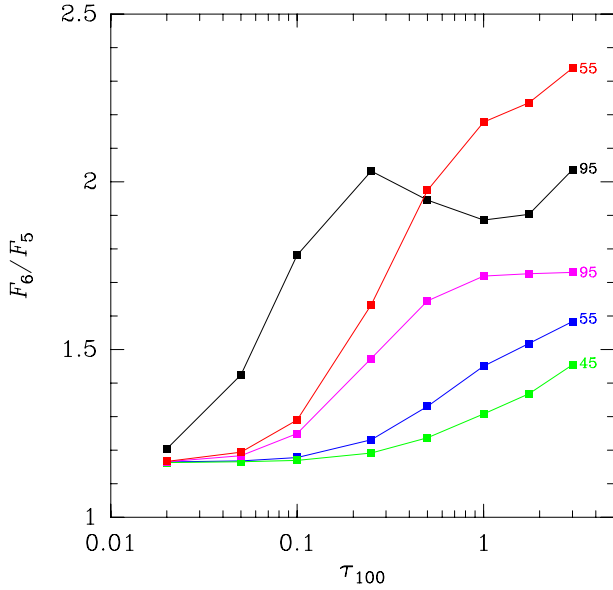
Fig. 6. F_6/F_5 (oH₂O $3_{21}-3_{12}$-to-$3_{12}-3_{03}$) line flux ratio as a function of τ_{100}. The small numbers on the right side of the curves indicate the values of T_{dust} for each curve. The H₂O column density per unit of velocity interval is $N_{\mathrm{H_2O}}/\Delta V = 10^{15}$ cm^{-2}/(km s^{-1}) (green, blue, and magenta curves) and $N_{\mathrm{H_2O}}/\Delta V = 5 \times 10^{15}$ cm^{-2}/(km s^{-1}) (red and black curves).

colder (dust) component enhances lines 2−4 (with probable contribution from collisionally excited gas, as suggested by the high F_2/F_3 ratio), can give a good fit to the SLED (G-A10), although the characteristics of the "cold" component (density, extension, T_{dust}) are relatively uncertain. A relatively low flux in line 4 can also be produced by absorption of continuum photons emanating from a very optically thick component, as in Arp 220 (see Appendix A).

4.3. The $L_{\mathrm{H_2O}} - L_{\mathrm{IR}}$ correlations

4.3.1. H₂O and the observed SED

It has long been recognized that single-temperature graybody fits to galaxy SEDs at far-IR wavelengths often underpredict the observed emission at $\lambda < 50$ μm. Therefore, multicomponent fitting, based on, for example, a two-temperature approach, a power-law mass-temperature distribution, a power-law mass-intensity distribution, or a single cold dust temperature graybody with a mid-IR power law (Dunne et al. 2003; Kóvacs et al. 2010; Dale & Helou 2002; Casey 2012), is required to match the full SED from the mid-IR to millimeter wavelengths. Our single-temperature model results on the H₂O SLED favors $T_{\mathrm{dust}} \gtrsim 45$ K (Sect. 4.2), significantly warmer than the cold dust temperatures (<40 K) that account for most of the observed far-IR emission in luminous IR galaxies, indicating that the H₂O submm emission primarily probes the warm region(s) of galaxies where the mid-IR (20−50 μm) emission is generated (see footnote 5).

Relative to the total IR emission of a galaxy, L_{IR}^T, the contribution to the luminosity by a given T_{dust} component i is $f_i = L_{\mathrm{IR}}^i/L_{\mathrm{IR}}^T$, and the observed H₂O-to-IR luminosity ratio is

$$\frac{L_{\mathrm{H_2O}}}{L_{\mathrm{IR}}^T} = \sum_i f_i \left(\frac{L_{\mathrm{H_2O}}}{L_{\mathrm{IR}}}\right)_i = f_{\mathrm{warm}} \left(\frac{L_{\mathrm{H_2O}}}{L_{\mathrm{IR}}}\right)_{\mathrm{warm}} + f_{\mathrm{cold}} \left(\frac{L_{\mathrm{H_2O}}}{L_{\mathrm{IR}}}\right)_{\mathrm{cold}} \quad (9)$$

where $(L_{\mathrm{H_2O}}/L_{\mathrm{IR}})_i$ are the values plotted in Figs. 3a2−f2 (for $\Delta V = 100$ km s^{-1}), and the problem is grossly simplified by
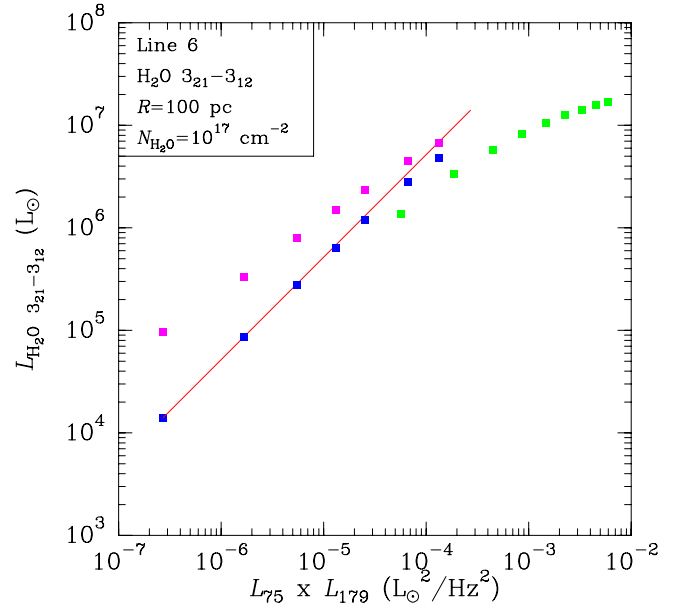

Fig. 7. Model results showing the luminosity of the H₂O line 6 ($3_{21}-3_{12}$) as a function of the product of the monochromatic luminosities at 75 and 179 μm. Luminosities are calculated for a source with $R_{\mathrm{eff}} = 100$ pc, $N_{\mathrm{H_2O}}/\Delta V = 10^{15}$ cm^{-2}/(km s^{-1}), and $\Delta V = 100$ km s^{-1}. Blue squares indicate models with $\tau_{100} = 0.1$, resulting in optically thin or moderately thick H₂O emission, without collisional excitation. Magenta squares show results for the same models but with collisional excitation included with $T_{\mathrm{gas}} = 150$ K and $n_{\mathrm{H_2}} = 3 \times 10^5$ cm^{-3}. Green symbols indicate models with $\tau_{100} = 1.0$, resulting in optically thick H₂O emission. For optically thin H₂O emission and without collisional excitation, the models indicate a linear correlation between $L_{\mathrm{H_2O}}$ and $L_{75} \times L_{179}$ (red line).

considering only two "warm" and "cold" components. From the comparison of the observed average SLED (Y13) with our models, we infer that the contribution by the cold component to $L_{\mathrm{H_2O}}/L_{\mathrm{IR}}^T$ is small, even though f_{cold} may be high. Since our modeled L_{IR} emission from the warm component is thus only a fraction, f_{warm}, of the total IR budget, the modeled $L_{\mathrm{H_2O}}/L_{\mathrm{IR}}$ ratios in Figs. 3a2−f2 should be considered upper limits. The value of f_{warm} can only be estimated by fitting the individual SEDs.

4.3.2. H₂O emission and monochromatic luminosities

The H₂O submm emission of lines 2−6 essentially involves two excitation processes, that of the base level (2_{12} for ortho and 1_{11} for para-H₂O) and absorption in the transitions at 75 μm (ortho) or 101 μm (para, Fig. 1). If collisional excitation is unimportant, the excitation of the base levels is also produced by absorption of dust-emitted photons in the corresponding transitions, i.e., in the $2_{12}-1_{01}$ line at 179 μm (ortho) or $1_{11}-0_{00}$ at 269 μm (para). In optically thin conditions and for fixed $N_{\mathrm{H_2O}}$ and ΔV, our models then show a linear correlation between the H₂O luminosities $L_{\mathrm{H_2O}}$ and the product of the continuum monochromatic luminosities responsible for the excitation, $L_{179} \times L_{75}$ (ortho) or $L_{269} \times L_{101}$ (para). This linear correlation is illustrated in Fig. 7 for line 6. The linear correlation, however, breaks down when the line becomes optically thick or when collisional excitation becomes important (in which case, $L_{\mathrm{H_2O}}$ is independent of $L_{179(269)}$).
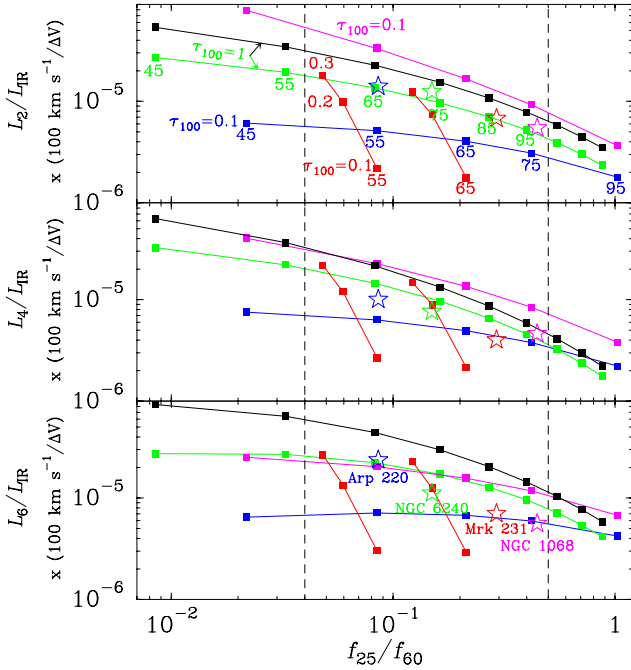
Fig. 8. Modeled $L_{H_2O}/L_{IR} \times (100 \text{ km s}^{-1}/\Delta V)$ for lines 2 (*upper*), 4 (*middle*), and 6 (*lower*) as a function of the f_{25}/f_{60} color. The dashed vertical lines indicate the lower and upper limits for f_{25}/f_{60} measured by Y13. In the *upper panel*, the small numbers below the squares indicate the value of T_{dust}, and τ_{100} is also indicated. Blue squares: $N_{H_2O}/\Delta V = 10^{15}$ cm^{-2}/(km s^{-1}) and $\tau_{100} = 0.1$; magenta: same as blue symbols but with collisional excitation included with $T_{gas} = 150$ K and $n_{H_2} = 3 \times 10^5$ cm^{-3}; green: $N_{H_2O}/\Delta V = 10^{15}$ cm^{-2}/(km s^{-1}) and $\tau_{100} = 1.0$; black: same as green but with $N_{H_2O}/\Delta V = 5 \times 10^{15}$ cm^{-2}/(km s^{-1}). Red squares show results for fixed $T_{dust} = 55$ and 65 K with $N_{H_2O}/(\Delta V \tau_{100}) = 5 \times 10^{15}$ cm^{-2}/(km s^{-1}) and $\tau_{100} = 0.1-0.3$. The starred symbols indicate the positions of Arp 220 (blue), NGC 6240 (green), Mrk 231 (red), and NGC 1068 (magenta), as reported by Rangwala et al. (2011), Meijerink et al. (2013), G-A10, and Y13, respectively. When compared with observations, the modeled L_{IR} values should be considered a fraction of the observed IR luminosities (Sect. 4.3.1). If f_{60} is contaminated by cold dust, the points would move to the left.

4.3.3. The L_{H_2O}/L_{IR} ratios and T_{dust}

The above considerations are relevant for our understanding of the behavior of the modeled L_{H_2O}/L_{IR} values with variations in T_{dust}. In the optically thin case and with collisional excitation ignored, the double dependence of L_{H_2O} on two monochromatic luminosities implies that L_{H_2O} is (nearly) proportional to L_{IR}. Our predicted SEDs indicate that, for small variations in T_{dust} around 55 K, $L_{269} \propto L_{IR}^{2/7}$ and $L_{101} \propto L_{IR}^{1/2}$. Therefore, for the para-H$_2$O lines 2–4, $L_{2-4} \propto L_{IR}^{0.8}$ in optically thin conditions, slightly slower than linear. For the ortho lines, $L_{179} \propto L_{IR}^{1/3}$ and $L_{75} \propto L_{IR}^{2/3}$, so that $L_{5-6} \propto L_{IR}$. This explains why, in Figs. 3a2–b2, the L_{2-4}/L_{IR} ratios show a slight decrease with increasing T_{dust} above 55 K, while L_{5-6}/L_{IR} versus T_{dust} attain a maximum at $T_{dust} \approx 55$ K in optically thin models that omit collisional excitation. These results are robust against variations in the spectral index of dust down to $\beta = 1.5$ (Sect. 3.1).

In Fig. 8 we show the L_{H_2O}/L_{IR} ratios (with $\Delta V = 100$ km s^{-1}; $L_{H_2O}/L_{IR} \propto \Delta V$) for lines 2, 4, and 6 as a function of the f_{25}/f_{60} color. The observed f_{25}/f_{60} was used by Y13 to characterize the H$_2$O emission and is especially relevant given that the H$_2$O submm emission arises in warm regions in which the mid-IR continuum emission is not severely contaminated by

cold dust. However, the continuum at $\lambda = 60$ μm may still be contaminated to some extent, in which case the data points in Fig. 8 will move toward the left. We also recall that the L_{H_2O}/L_{IR} values are upper limits.

The first conclusion inferred from Fig. 8 is that the range of f_{25}/f_{60} colors measured by Y13 (between the dashed lines) matches T_{dust} in the ranges favored by the observed H$_2$O line flux ratios, that is, 50–75 K and optically thin conditions ($\tau_{100} = 0.1$) and also $T_{dust} = 60-95$ K and $\tau_{100} = 1.0$. This indicates that the warm environments responsible for the H$_2$O emission are best traced in the continuum in this wavelength range, but also that the f_{25}/f_{60} color alone involves degeneracy in the dominant T_{dust} and τ_{100} responsible for the mid-IR continuum emission. As shown in Sect. 4.2, the first set of conditions can explain the line ratios 2–6 in warm sources (where lines 7–8 are not detected to a significant level), while the second set is required to explain the H$_2$O emission in very warm sources (with detection of lines 7–8).

Second, it is also relevant that the L_{H_2O}/L_{IR} values differ by a factor $\lesssim 2$ between models with warm dust in the optically thin regime ($T_{dust} = 55$ K, $\tau_{100} = 0.1$, $N_{H_2O}/\Delta V = 10^{15}$ cm^{-2}/(km s^{-1})) and those with very warm dust in the optically thick regime with high H$_2$O columns ($T_{dust} = 95$ K, $\tau_{100} = 1$, $N_{H_2O}/\Delta V = 5 \times 10^{15}$ cm^{-2}/(km s^{-1})), potentially explaining why sources with different physical conditions show similar L_{H_2O}/L_{IR} ratios (Y13).

Third, in optically thin conditions ($\tau_{100} \sim 0.1$) and if collisional excitation is unimportant, the models with constant $N_{H_2O}/\Delta V = 10^{15}$ cm^{-2}/(km s^{-1}) (blue symbols) predict a slow decrease in L_{2-4}/L_{IR} and a nearly constant L_{5-6}/L_{IR} with increasing f_{25}/f_{60}, as argued above. This behavior, however, fails to match the observed trends (Y13), as L_{2-4}/L_{IR} and L_6/L_{IR} decrease by factors of ~ 2 and ~ 3, respectively, when f_{25}/f_{60} increases from $\lesssim 0.08$ to $\gtrsim 0.15$. When collisional excitation is included (magenta symbols), the L_{2-4}/L_{IR} ratios show a stronger dependence on f_{25}/f_{60}, but L_6/L_{IR} still changes only slightly with f_{25}/f_{60}.

Therefore, optically thin models with varying T_{dust} but constant τ_{100}, $N_{H_2O}/\Delta V$, and ΔV cannot account for the observed $L_{H_2O}/L_{IR} - f_{25}/f_{60}$ trend. This indicates that, in optically thin galaxies, parameters other than T_{dust} are systematically varied when f_{25}/f_{60} is increased and that optically thick sources also contribute to the observed trend:

(i) Galaxies in the optically thin regime (with $\tau_{100} < 1$) are predicted to show a very steep dependence of L_{H_2O}/L_{IR} on τ_{100} for constant T_{dust} and $N_{H_2O}/(\Delta V \tau_{100})$ (that is, for constant H$_2$O abundance), with higher τ_{100} impling *lower* f_{25}/f_{60}. We illustrate this point in Fig. 8 with the red squares, corresponding to fix $T_{dust} = 55$ and 65 K and $N_{H_2O}/(\Delta V \tau_{100}) = 5 \times 10^{15}$ cm^{-2}/(km s^{-1}), with τ_{100} ranging from 0.1 to 0.3. Therefore, we expect that the observed increase in f_{25}/f_{60} is not only due to an increase in T_{dust} from source to source, but also to variations in τ_{100} in the optically thin regime. Examples of galaxies in this regime are the AGNs NGC 6240 and NGC 1068 (see also Appendix A).

(ii) In the optically thick regime ($\tau_{100} \gtrsim 1$), galaxies are also predicted to show a relatively steep variation in L_{H_2O}/L_{IR} with f_{25}/f_{60} due to increasing T_{dust} (black symbols in Fig. 8) because the H$_2$O lines saturate and their luminosities flatten with increasing monochromatic luminosities (Fig. 7). Extreme examples of this galaxy population are Arp 220 and Mrk 231. Line saturation also implies that the L_{H_2O}/L_{IR} ratios are not much higher than in the optically thin case
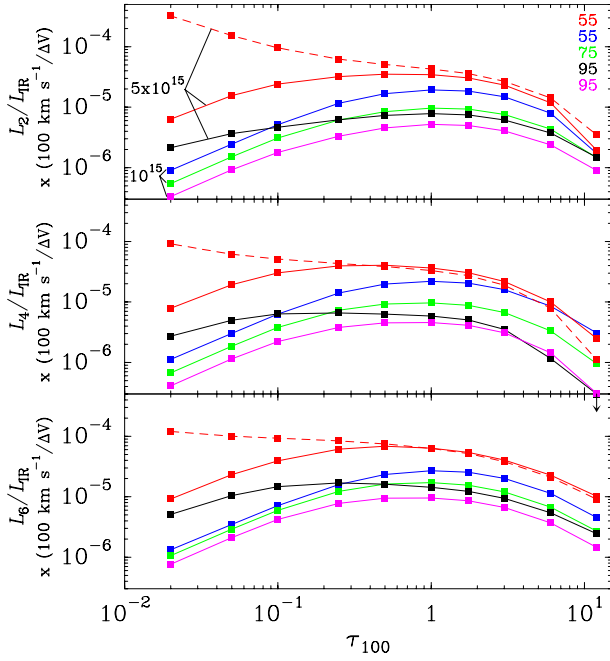
Fig. 9. Modeled $L_{H_2O}/L_{IR} \times (100\,km\,s^{-1}/\Delta V)$ values for lines 2 (*upper*), 4 (*middle*), and 6 (*lower*) as a function of τ_{100}. Collisional excitation is ignored except for the red dashed lines, where $T_{gas} = 150$ K and $n_{H_2} = 3 \times 10^5$ cm^{-3} are adopted. The small numbers on the right side of the upper panel indicate the value of T_{dust} in K, and those on the left side indicate $N_{H_2O}/\Delta V$ in cm^{-2}/(km s^{-1}). When compared with observations, the modeled L_{IR} values should be considered a fraction of the observed IR luminosities (Sect. 4.3.1). For $\tau_{100} = 12$ and $T_{dust} = 95$ K, line 4 is predicted to be in absorption. For fixed T_{dust} and $\tau_{100} \sim 1$, the L_{H_2O}/L_{IR} ratios are similar for very different N_{H_2O}, indicating line saturation.

even if much higher $N_{H_2O}/\Delta V = 5 \times 10^{15}$ cm^{-2}/(km s^{-1}) are present, and the corresponding ratios are consistent with the observed values to within the uncertainties in f_{warm}. The presence of even warmer dust (>100 K) with significant contribution to L_{IR} will additionally decrease L_{H_2O}/L_{IR} (Y13).

In summary, the steep decrease in L_{H_2O}/L_{IR} at $f_{25}/f_{60} \approx$ 0.1−0.15 measured by Y13 is consistent with both types of galaxies (with optically thin and optically thick continuum) populating the diagram and suggests that the observed variations in f_{25}/f_{60} are not only due to variations in T_{dust} but also to variations in τ_{100} in the optically thin regime. At the other extreme, the optically thick (saturated) and very warm galaxies are also expected to show a decrease in L_{H_2O}/L_{IR} with increasing T_{dust} (and f_{25}/f_{60}), as anticipated by Y13. To distinguish between both regimes for a given galaxy, the line ratios (specifically F_6/F_5, Sect. 4.2) and mostly the detection of lines 7−8 or the detection of high-lying H$_2$O absorption lines at far-IR wavelengths are required. The observations reported by Y13 indicate that these optically thick and warm components (diagnosed by the detection of lines 7−8) are present in at least ten sources. At least in NGC 1068 the upper limits on lines 7−8 are stringent (S12), allowing us to infer optically thin conditions.

4.3.4. Line saturation and a theoretical upper limit to L_{H_2O}/L_{IR}

Saturation of the H$_2$O submm lines in optically thick ($\tau_{100} \sim$ 1) sources implies that there is an upper limit on $L_{H_2O}/L_{IR} \times (100\,km\,s^{-1}/\Delta V)$ that, in the absence of significant collisional

excitation, cannot be exceeded. In Fig. 9, the $L_{H_2O}/L_{IR} \times (100\,km\,s^{-1}/\Delta V)$ ratios for lines 2, 4, and 6 are plotted as a function of τ_{100} for the most favored T_{dust} range of 55−95 K and $N_{H_2O}/\Delta V = (1-5) \times 10^{15}$ cm^{-2}/(km s^{-1}). In optically thin conditions ($\tau_{100} \lesssim 0.1$ for $N_{H_2O}/\Delta V = 10^{15}$ cm^{-2}/(km s^{-1})) and without collisions, L_{H_2O}/L_{IR} scales linearly (for fixed ΔV) with τ_{100} because $L_{179(269)} \times L_{75(101)} \propto \tau_{100}^2$ while $L_{IR} \propto \tau_{100}$. The curves flatten as the H$_2$O lines saturate and show a maximum at $\tau_{100} \approx 0.5-1$. Values of τ_{100} significantly higher than unity are predicted to decrease L_{H_2O}/L_{IR}. In very optically thick components of very warm sources, the submm lines are predicted to be observed in weak emission or even in absorption, especially in line 4. Arp 220 is a case in point (Sakamoto et al. 2008), in which the H$_2$O submm emission is expected to arise from a region that surrounds the optically thick nuclei (see Appendix A). For $\Delta V = 100$ km s^{-1}, the maximum attainable values of L_{H_2O}/L_{IR} (red curves) are 3.5×10^{-5}, 4×10^{-5}, and 7×10^{-5} for lines 2, 4, and 6, respectively, comfortably higher than the values observed in any source by Y13. Recently, a value of $L_2/L_{IR} = (4.3 \pm 1.6) \times 10^{-5}$ has been measured in the submillimeter galaxy SPT 0538-50, a gravitationally lensed dusty star-forming galaxy at $z \approx 2.8$ (Bothwell et al. 2013). Although the authors do not exclude differential lensing effects, which could affect the line-to-luminosity ratios, this value is still consistent with our upper limit, suggesting strong saturation in this source. In HFLS3 at $z = 6.34$, Riechers et al. (2013) have measured $F_6/F_2 = 2.2 \pm 0.5$ and $F_6/F_5 = 2.6 \pm 0.8$; within the uncertainties, these values are consistent with warm or very warm $T_{dust} \gtrsim 65$ K and high N_{H_2O} (Figs. 5, 6). The H$_2$O lines are most likely saturated in HFLS3 as is also indicated by the $L_6/L_{IR} = (7.7 \pm 1.3) \times 10^{-5}$ ratio, which is still consistent with the strong saturation limit for warm T_{dust} given the very broad linewidth of the H$_2$O line (~940 km s^{-1}; see Sect 3.2). O13 reported $L_2/L_{IR} = (0.5 - 2) \times 10^{-5}$ in high-z ultra-luminous infrared galaxies, also consistent with the upper limit in Fig. 9 even for $T_{dust} \sim 75$ K when taking the broad line widths of the H$_2$O lines into account. Line saturation and a relatively small contribution from cold dust to the infrared emission in these extreme galaxies are implied. With collisional excitation in optically thin environments with moderate T_{dust} but high N_{H_2O}, the above L_{H_2O}/L_{IR} ratios (red dashed lines in Fig. 9) may even attain higher values, though the adopted $\Delta V = 100$ km s^{-1} is too high for $\tau_{100} < 0.3$ and $n_{H_2} = 3 \times 10^5$ cm^{-3} (Sect 3.2, Eq. (6)).

4.3.5. The correlation

The broad range in observed L_{IR} in luminous IR galaxies with H$_2$O emission may be attributable to varying the effective size of the emitting region. As noted in Sect. 3.2, varying R_{eff} (equivalent to varying the number of individual regions that contribute to L_{IR} or to increasing L_{IR} for a single source) is expected to generate linear $L_{H_2O} - L_{IR}$ correlations if the other parameters (T_{dust}, τ_{100}, T_{gas}, n_{H_2}, $N_{H_2O}/\Delta V$, and ΔV) remain constant.

In Fig. 10 we show the L_2/L_{IR} ratio as a function of τ_{100} for models with $T_{dust} = 55$ K and $T_{dust} = 75$ K that assume a constant H$_2$O-to-dust opacity ratio, that is, $N_{H_2O}/\tau_{100} = 10^{18}$ cm^{-2}. According to Eq. (1), this corresponds to a constant H$_2$O abundance of 7.7×10^{-7}. Both models with $\Delta V = 100$ km s^{-1} (independent of τ_{100}), and $\Delta V/\tau_{100} = 100$ km s^{-1} (corresponding to a constant $K_{vir} = 1.3$) are shown. The figure illustrates that a supralinear correlation between L_{H_2O} and L_{IR} can be expected if, on average, τ_{100} is an increasing function of L_{IR}. If most sources with $L_{IR} \sim 5 \times 10^{10}$ $L_\odot$ were optically thin ($\tau_{100} \sim 0.1$), and the high-z sources with $L_{IR} \sim 10^{13}$ $L_\odot$ (O13) were mostly
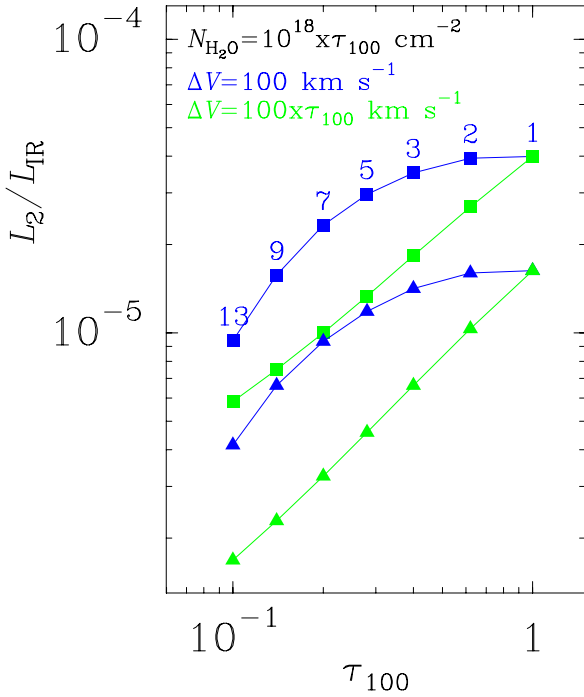
Fig. 10. Modeled L_2/L_{IR} ratio as a function of τ_{100}. Squares and triangles indicate $T_{dust} = 55$ and 75 K, respectively. In all models, collisional excitation is included with $T_{gas} = 150$ K and $n_{H_2} = 3 \times 10^4$ cm^{-3}. $N_{H_2O}/\tau_{100} = 10^{18}$ cm^{-2} is adopted, corresponding to a constant H_2O abundance of 7.7×10^{-7} (Eq. (1)). Blue symbols indicate models with $\Delta V = 100$ km s^{-1} and thus with variable K_{vir} (Eq. (5)) indicated with the numbers. Green symbols show results with $\Delta V = 100 \times \tau_{100}$ km s^{-1} simulating a constant value of $K_{vir} = 1.3$. When compared with observations, the modeled L_{IR} values should be considered a fraction of the observed IR luminosities (Sect. 4.3.1), and thus the modeled L_2/L_{IR} values are upper limits.

optically thick ($\tau_{100} \sim 1$), one would then expect $L_2 \propto L_{IR}^{1.3}$ from Fig. 10, which can account for the observed supralinear correlation found by O13 and Y13. However, similar supralinear correlations would then be expected for the other submm lines 3−6.

5. Summary of the model results for optically classified starbursts and AGNs

Following the classification of sources by Y13 into optically classified star-formation-dominated galaxies with possible mild AGN contribution (HII+mild AGN sources) and optically identified strong-AGN sources, we now consider these two groups separately.

5.1. HII+mild AGN sources

We focus here on those HII+mild AGN sources where lines 2−6 are detected but lines 7−8 are undetected (that is, "warm" sources as defined in Sect. 4.1). The average H_2O flux ratios reported by Y13 (their Table 2) indicate that (i) $F_6/F_2 \sim 1.2$, favoring $T_{dust} = 55$ K if there is no significant collisional excitation and $T_{dust} = 75$ K if the H_2O emission arises in warm and dense gas (Fig. 5); (ii) $F_6/F_5 \sim 1.2$, consistent with the optically thin regime (Fig. 6). For these T_{dust}, Fig. 11a shows the values of N_{H_2O} for $\Delta V = 100$ km s^{-1} required to explain the observed L_{H_2O}/L_{IR} ratios, as a function of τ_{100}. Models with included or excluded collisional excitation are considered. We

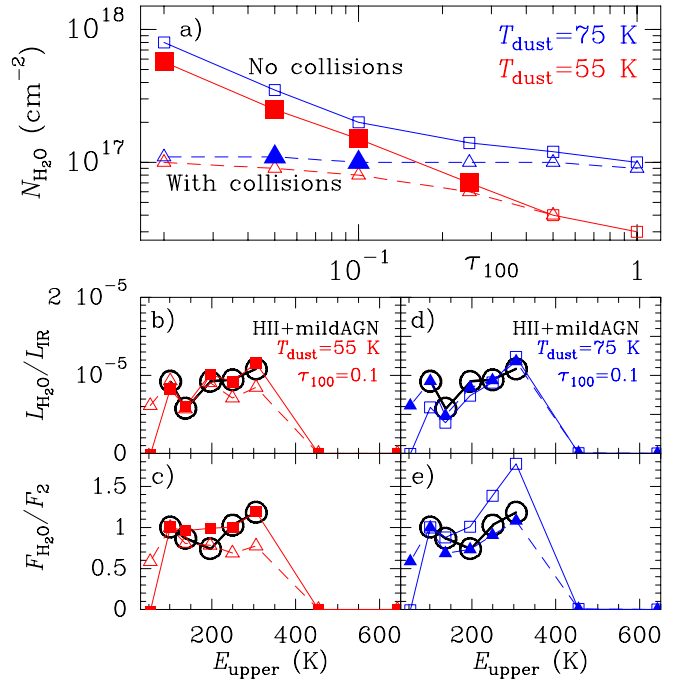**Fig. 11.** **a)** Values of N_{H_2O} for $\Delta V = 100$ km s^{-1} as a function of τ_{100}, for $T_{dust} = 55$ K (red) and 75 K (blue), required to account for the observed averaged L_{H_2O}/L_{IR} ratios in HII-mild AGN sources (as given by Y13). Models both without (squares) and with (triangles) collisional excitation are shown. In the latter models, $T_{gas} = 150$ K, and $n_{H_2} = 5 \times 10^4 - 3 \times 10^5$ cm^{-3} for $T_{dust} = 55 - 75$ K, respectively. The large filled symbols indicate the best fit models to the averaged SLED. Panels **b)**−**e)** compare in detail the four models with $\tau_{100} = 0.1$ (both with and without collisions) with the observed values (black circles) in HII-mild AGN sources (both the normalized flux ratios (SLED) and the L_{H_2O}/L_{IR} ratios, Y13, for lines 2−6). In panels **b)** and **d)**, the models indicate the values of L_{H_2O}/L_{IR} for $\Delta V = 100$ km s^{-1}. Lines 1, 7, and 8 are excluded from the comparison because of their low detection rates (Y13).

recall that ΔV is the velocity dispersion of the dominant structure(s) that accounts for the H_2O emission (Sect. 3.2), and for the case of low τ_{100} and relatively high densities, Eq. (6) suggests $\Delta V < 100$ km s^{-1} with the consequent increase in N_{H_2O} (Fig. 10).

The decrease in τ_{100} implies the increase in N_{H_2O} in optically thin conditions and when collisional excitation is unimportant. Our best fit models for the average SLED (big solid symbols) favor optically thin far-IR emission ($\tau_{100} \lesssim 0.3$). In Figs. 11b−e, the detailed comparison between the $\tau_{100} = 0.1$ models and the observations (Y13) is shown. Significant collisional excitation is not favored for $T_{dust} = 55$ K, since it would increase F_2 relative to F_6. In addition, these optically thin models have the drawback of overestimating F_4/F_2. Conversely, the $T_{dust} = 75$ K models favor significant collisional excitation in order to increase F_2 relative to F_6. The very optically thin models ($\tau_{100} \lesssim 0.05$) are also not favored given the very high amounts of H_2O required to explain (with no collisional excitation) the L_{H_2O}/L_{IR} ratios.

In summary, $T_{dust} = 55 - 75$ K, $\tau_{100} \sim 0.1$, and $N_{H_2O} \sim (0.5 - 2) \times 10^{17}$ cm^{-2} can explain the bulk of the H_2O submm emission in warm star-forming galaxies (Table 2). As shown in Fig. 8, $T_{dust} = 55$ K and $\tau_{100} = 0.1 - 0.2$ predict 25-to-60 μm flux density ratios of $f_{25}/f_{60} = (8.5 - 6.0) \times 10^{-2}$, in agreement with the observed values for the bulk of sources (Y13), while $T_{dust} = 75$ K and $\tau_{100} = 0.1 - 0.2$ predict $f_{25}/f_{60} = 0.42 - 0.30$ (close to the observed upper values). Assuming a gas-to-dust ratio of 100 by mass, $\tau_{100} \sim 0.1$ corresponds to a column density

of H nuclei of $N_H \approx 1.3 \times 10^{23}$ cm^{-2} (Eq. (1)), and thus an H_2O abundance of $X_{H_2O} \sim 10^{-6}$. To within a factor of 3 uncertainty due to the $\tau_{100} - N_H$ calibration, the specific values used for τ_{100} and ΔV, and variations in the measurements for individual sources, this is the typical H_2O abundance that we infer from the observed $L_{H_2O} - L_{IR}$ correlation. Molecular shocks and hot core chemistry are very likely responsible for this X_{H_2O}, which is well above the volume-averaged values inferred in Galactic dark clouds and PDRs (e.g., Bergin et al. 2000; Snell et al. 2000; Melnick & Bergin 2005; van Dishoeck et al. 2011).

Finally, we note that $T_{dust} = 55$ K and $\tau_{100} = 0.1-0.2$, and the assumption that most of the IR is powered by star formation in these sources of Y13, imply a star-formation-rate surface density[7] of $\Sigma_{SFR} = 121-195$ $M_\odot$ yr^{-1} kpc^{-2} and gas mass surface density of $\Sigma_{gas} = 1430-2860$ $M_\odot$ pc^{-2}. The implied depletion or exhaustion time scale, $t_{dep} = \Sigma_{gas}/\Sigma_{SFR}$, is ~12–15 Myr. These values lie close to the $\Sigma_{SFR} - \Sigma_{dense}$ star-formation correlation found by García-Burillo et al. (2012) from HCN emission in (U)LIRGs with their revised HCN-M_{dense} conversion factors. This agreement suggests that the submm H_2O and the mm HCN emission in (U)LIRGs arise from the same regions. Sources with $T_{dust} = 75$ K would imply even shorter time scales and suggest high rates of ISM return from SNe and stellar winds. A follow-up study of the relationship between L_{H_2O} and L_{HCN} is required to check this point. In addition, modeling the individual sources simultaneously in the continuum and the H_2O emission will provide further constraints on the nature of these regions.

5.2. Strong optically classified AGN sources

The general finding that the H_2O emission is similar in star-forming and strong-AGN sources (Y13) may simply indicate that the far-IR pumping of H_2O occurs regardless of whether the dust is heated via star formation or an AGN. There are, however, some differences between the two source types. Strong AGNs show a higher detection rate in H_2O $1_{11}-0_{00}$ (Y13), indicating that the gas densities are higher in the circumnuclear regions of AGNs. Another difference is that the L_{H_2O}/L_{IR} ratios are somewhat lower in strong AGN sources (Y13). While relatively low columns of dust and H_2O in these sources could explain this observational result, it is also possible that high X-ray fluxes photodissociate H_2O, reducing its abundance relative to star-forming galaxies. High abundances of H_2O require effective shielding from UV and X-ray photons and thus high columns of dust and gas that, in AGN-dominated galaxies, may be effectively provided by an optically thick torus probably accompanied by starburst activity. In addition, warm dust further enhances X_{H_2O} through an undepleted chemistry and pumps the excited H_2O levels, while warm gas will further boost X_{H_2O} through reactions of OH with H_2. These appear to be the ideal conditions for the presence of large quantities of H_2O in the (circum)nuclear regions of galaxies.

has made use of NASA's Astrophysics Data System (ADS) and of GILDAS software (http://www.iram.fr/IRAMFR/GILDAS).

References

Appleton, P. N., Guillard, P., Boulanger, F., et al. 2013, ApJ, 777, 66
Bergin, E. A., Melnick, G. J., Stauffer, J. R., et al. 2000, ApJ, 539, L129
Bothwell, M. S., Aguirre, J. E., Chapman, S. C., et al. 2013, ApJ, 779, 67
Bradford, C. M., Bolatto, A. D., Maloney, P. R., et al. 2011, ApJ, 741, L37
Bryant, P. M., & Scoville, N. Z. 1996, ApJ, 457, 678
Casey, C. M. 2012, MNRAS, 425, 3094
Chabrier, G. 2003, ApJ, 586, L133
Combes, F., Rex, M., Rawle, T. D., et al. 2012, A&A, 538, L4
Dale, D. A., & Helou, G. 2002, ApJ, 576, 159
Daniel, F., Dubernet, M.-L., & Grosjean, A. 2011, A&A, 536, A76
Downes, D., & Eckart, A. 2007, A&A, 468, L57
Downes, D. & Solomon, P. M. 1998, ApJ, 507, 615
Draine, B. T. 1985, ApJS, 57, 587
Dubernet, M.-L., Daniel, F., Grosjean, A., & Lin, C. Y. 2009, A&A, 497, 911
Dunne, L., Eales, S. A., & Edmunds, M. G. 2013, MNRAS, 341, 589
Fischer, J., Luhman, M. L., Satyapal, S., et al. 1999, Ap&SS, 266, 91
Fischer, J., Sturm, E., González-Alfonso, E., et al. 2010, A&A, 518, L41
Gao, Y., & Solomon, P. M. 2004a, ApJ, 606, 271
Gao, Y., & Solomon, P. M. 2004b, ApJS, 152, 63
García-Burillo, S., Usero, A., Alonso-Herrero, A., et al. 2012, A&A, 539, A8
Goldsmith, P. F. 2001, ApJ, 557, 736
González-Alfonso, E., Smith, H. A., Fischer, J., & Cernicharo, J. 2004, ApJ, 613, 247
González-Alfonso, E., Smith, H. A., Ashby, M. L. N., et al. 2008, ApJ, 675, 303
González-Alfonso, E., Fischer, J., Isaak, K., et al. 2010, A&A, 518, L43
González-Alfonso, E., Fischer, J., Graciá-Carpio, J., et al. 2012, A&A, 541, A4 (G-A12)
González-Alfonso, E., Fischer, J., Bruderer, S., et al. 2013, A&A, 550, A25
González-Alfonso, E., Fischer, J., Graciá-Carpio, J., et al. 2014, A&A, 561, A27
Griffin, M. J., Abergel, A., Abreu, A., et al. 2010, A&A, 518, L3
Hailey-Dunsheath, S., Sturm, E., Fischer, J., et al. 2012, ApJ, 755, 57 (H12)
Impellizzeri, C. M. V., McKean, J. P., Castangia, P., et al. 2008, Nature, 456, 927
Kóvacs, A., Omont, A., Beelen, A., et al. 2010, ApJ, 717, 29
Krips, M., Martín, S., Eckart, A., et al. 2011, ApJ, 736, 37
Lis, D. C., Neufeld, D. A., Phillips, T. G., Gerin, M., & Neri, R. 2011, ApJ, 738, L6
Lupu, R. E., Scott, K. S., Aguirre, J. E., et al. 2012, ApJ, 757, 135
Meijerink, R., Kristensen, L. E., Weiß, A., et al. 2013, ApJ, 762, L16
Melnick, G. J., & Bergin, E. A. 2005, Adv. Space Res., 36, 1027
Müller, H. S. P., Thorwirth, S., Roth, D. A., & Winnewisser, G. 2001, A&A, 370, L49
Müller, H. S. P., Schlöder, F., Stutzki, J., & Winnewisser, G. 2005, J. Mol. Struct., 742, 215
Omont, A., Neri, R., Cox, P., et al. 2011, A&A, 530, L3
Omont, A., Yang, C., Cox, P., et al. 2013, A&A, 551, A115 (O13)
Papadopoulos, P. P., & Seaquist, E. R. 1999, ApJ, 516, 114
Papadopoulos, P. P., Isaak, K. G., & van der Werf, P. P. 2007, ApJ, 668, 815
Pereira-Santaella, M., Spinoglio, L., & Busquet, G., et al. 2013, ApJ, 768, 55
Pickett, H. M., Poynter, R. L., Cohen, E. A., et al. 1998, J. Quant. Spectr. Rad. Transf., 60, 883
Pilbratt, G. L., Riedinger, J. R., Passvogel, T., et al. 2010, A&A, 518, L1
Poglitsch, A., Waelkens, C., Geis, N., et al. 2010, A&A, 518, L2
Preibisch, Th., Ossenkopf, V., Yorke, H.W., & Henning, Th. 1993, A&A, 279, 577
Rangwala, N., Maloney, P. R., Glenn, J., et al. 2011, ApJ, 743, 94
Riechers, D. A., Bradford, C. M., Clements, D. L., et al. 2013, Nature, 496, 329
Sakamoto, K., Wang, J., Wiedner, M. C., et al. 2008, ApJ, 684, 957
Snell, R. L., Howe, J. E., Ashby, M. L. N., et al. 2000, ApJ, 539, L101
Spinoglio, L., Pereira-Santaella, M., Busquet, G., et al. 2012, ApJ, 758, 108 (S12)
van der Werf, P. P., Isaak, K. G., Meijerink, R., et al. 2010, A&A, 518, L42
van der Werf, P., Berciano Alba, A., Spaans, M., et al. 2011, ApJ, 741, L38
van Dishoeck, E. F., Kristensen, L. E., Benz, A. O., et al. 2011, PASP, 123,138
Yang C., Gao, Y., Omont, A., et al. 2013, ApJ, 771, L24 (Y13)

---

[7] Σ_{SFR} is estimated as $10^{-10} L_{IR}/(\pi R^2)$, where a Chabrier (2003) initial mass function is used, and Σ_{gas} is given by $M_{gas}/(\pi R^2)$ where $M_{gas} = \frac{4\pi}{3} N_H m_H R^2$ with $N_H = 1.3 \times 10^{24} \tau_{100}$ cm^{-2} (Eq. (1)).
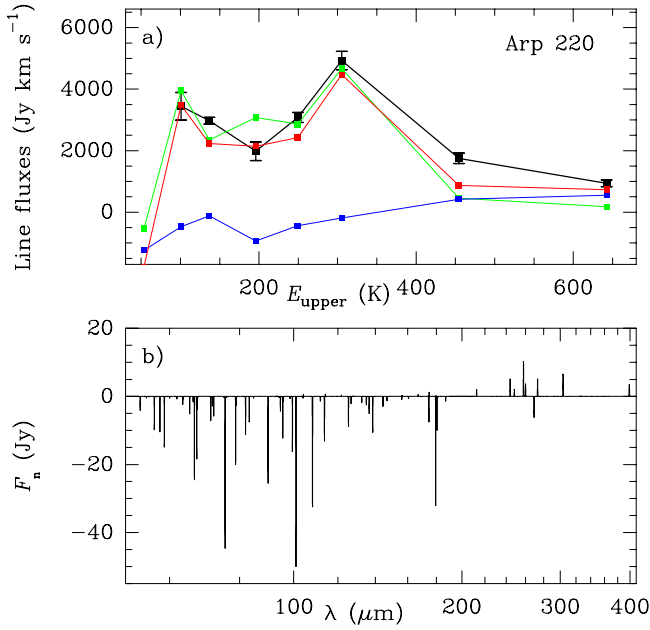
Fig. A.1. a) Proposed composite model for the H_2O submm lines in Arp 220 (see G-A12), compared with the observed line fluxes (black squares, from Rangwala et al. 2011). Toward the far-IR optically thick nuclear region (blue symbols), the $E_{upper} < 400$ K lines are expected mostly in absorption. The H_2O emission is generated around that nuclear region, in the $C_{extended}$ (G-A12) component (green). Red is total. **b)** Resulting predicted composite PACS/SPIRE H_2O continuum-subtracted spectrum of Arp 220, which is dominated by absorption of the continuum.

Appendix A: Two opposite, extreme cases: Arp 220 and NGC 1068

Arp 220 and NGC 1068 are prototypical sources that have been observed at essentially all wavelengths. With regard to their H_2O submm emission, these galaxies are extreme cases and deserve special consideration.

In the nearby ULIRG Arp 220, discrepancies between the observed SLED (Rangwala et al. 2011, Y13) and the single-component models of Figs. 3a1−c1 are worth noting. The observed high $L_6/L_{IR} \approx 2.4 \times 10^{-5}$ (Fig. 8), together with the high 6/2 ratio of ≈ 1.4 (Fig. A.1a), suggest $T_{dust} \gtrsim 65$ K and $N_{H_2O} \gtrsim 10^{17}$ cm^{-2}, consistent with detection of lines 7−8. However, high T_{dust} and N_{H_2O} are mostly compatible with $F_4/F_3 > 1$, while the observed ratio is ≈ 0.7 (Fig. A.1a). As in Mrk 231, a composite model is required to account for the H_2O SLED in this galaxy.

In sources with very optically thick and very warm cores such as Arp 220 (G-A12), the increase in τ_{100} above 1 decreases the submm H_2O fluxes due to the rise of submm extinction (Fig. 9). While higher T_{dust} generates warmer SEDs, but lowers the L_{H_2O}/L_{IR} ratios for lines 2−6, the increase in τ_{100} further decreases L_{H_2O}/L_{IR}. This behavior suggests that the optimal environments for efficient H_2O submm line emission are regions with high far-IR radiation density but moderate extinction, i.e., those that *surround* the thick core(s) where the bulk of the continuum emission is generated. In contrast, the H_2O absorption at shorter wavelengths is more efficiently produced in the near-side layers of the optically thick cores, primarily if high-lying lines are involved. Absorption and emission lines are thus complementary, providing information on the source structure.

We have taken the models in G-A12 for Arp 220 to predict its submm H_2O emission. In Fig. A.1a, the blue symbols/line
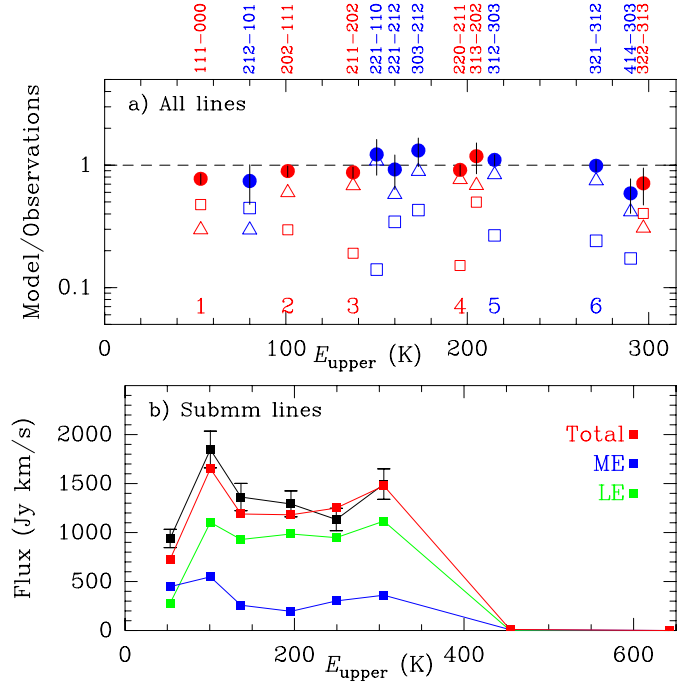

Fig. A.2. a) Composite model for the H_2O emission in NGC 1068 favored in this work. Blue/red indicate ortho/para lines, and the submm H_2O 1−6 lines (Table 1) are indicated. Open squares and triangles show the contribution by a moderate-excitation (ME) and a low-excitation (LE) component, and filled symbols indicate the total emission (see text for details); in both cases the submm H_2O lines 2−6 are pumped through far-IR photons emitted by dust. **b)** Comparison between the observed fluxes of the H_2O submm lines (black squares, from Spinoglio et al. 2012) and those predicted with the composite model.

indicate the predicted H_2O fluxes towards the optically thick, warm nuclear region (both C_{west} and C_{east}, see G-A12), indicating that most submm lines (with the exception of lines 3, 7, and 8) are predicted in absorption. The observed H_2O submm line emission (Rangwala et al. 2011) must therefore arise in the surrounding, optically thinner region, i.e., the $C_{extended}$ component, where the H_2O abundance in the inner parts ($R \lesssim 150$ pc, where $T_{dust} = 70-90$ K) is increased relative to G-A12 (so $C_{extended}$ has $N_{H_2O} = 1.3 \times 10^{17}$ cm^{-2} in Fig. A.1a). According to our model, the relatively low flux in line 4 is due to line absorption towards the nuclei. The main drawback of the model in Fig. A.1a is that line 7 is underestimated by a factor 2. The submm H_2O emission in Arp 220 traces a transition region between the compact optically thick cores and the extended kpc-scale disk (G-A12). The overall H_2O spectrum is, however, dominated by absorption of the continuum (Fig. A.1b).

Just the opposite set of conditions characterizes the nearby Seyfert 2 galaxy NGC 1068, since the nuclear continuum emission is optically thin and collisional excitation is important (S12). All detected H_2O lines, including those in the far-IR (100−200 μm) are seen in emission, and most of them show fluxes (in erg/s/cm^2) unrelated to wavelength, upper level energy (up to ≈ 300 K), or A-Einstein coefficient (S12). In particular, the H_2O $2_{21}-1_{10}$ (108 μm) and $2_{21}-2_{12}$ (180 μm) lines share the same upper level and show similar fluxes but the A-Einstein coefficient of the 108 μm transition is a factor of 8.4 higher than that of the 180 μm transition. With pure collisional excitation, the only way to account for the observed line ratios is to invoke high densities and H_2O column densities, but also a relatively low T_{gas} to avoid significantly populating the high-lying levels

(>300 K). S12 found that T_{gas} ~ 40 K, and very high N_{H_2O} and n_{H_2} can provide a reasonable fit to the SLED. However, these conditions are unrelated to the warmer gas conditions in the nuclear region of NGC 1068, as derived from the CO SLED (S12, Hailey-Dunsheath et al. 2012, hereafter H12). In addition, the observed H$_2$O submm SLED (Fig. A.2) is fairly similar to the SLEDs obtained in optically thin models with significant collisional excitation of the low-lying levels.

We have explored an alternative composite solution for the H$_2$O emission in NGC 1068 with lower densities and H$_2$O columns and higher T_{gas}, based on the far-IR pumping of the lines by an external *anisotropic* radiation field. In this framework, we can account for the weakness of the 108 μm line by the absorption of continuum photons, and indeed we would have to explain why this line is not observed to be even weaker than it is or in absorption. The higher lying far-IR $3_{22}-3_{13}$ emission line at 156.2 μm is in this scenario pumped through absorption of continuum photons in the $3_{22}-2_{11}$ line at 90 μm.

For the first component, we closely follow H12 in modeling the moderate-excitation (ME) component as an ensemble of clumps, which are described by T_{dust} = 55 K, τ_{100} = 0.18, $n_{H_2} = 10^6$ cm^{-3}, T_{gas} = 150 K, and $N_{H_2O} = 6.5 \times 10^{16}$ cm^{-2}, and V_{turb} = 15 km s^{-1} (giving K_{vir} ~ 10, see H12). With a mass of 7.5×10^6 $M_{\odot}$, this component is unable to account for the H$_2$O submm lines 2−6, but generates a significant fraction of the observed emission in line 1 and some far-IR lines (Fig. A.2a and panel b).

We then added another, low-excitation (LE) component, which is identified with the gas generating the low-J CO lines (Krips et al. 2011, S12) and is thus assigned a density of $n_{H_2} = 2 \times 10^4$ cm^{-3}. For simplicity, we also assume T_{dust} = 55 K, τ_{100} = 0.18, and $N_{H_2O} = 6.5 \times 10^{16}$ cm^{-2} as for the ME, but adopt the higher V_{turb} of 60 km s^{-1} (giving K_{vir} ~ 7). For the LE component, and besides the *internal* far-IR field described by its T_{dust} and τ_{100}, we also follow H12 in including an *external* field (associated with the emission from the whole region), which is described as a graybody with T_{BG} = 55 K and τ_{100}^{BG} = 0.05. The resulting mean specific intensity at 100 μm of the external field, $J_{ext}^{100 \, \mu m}$, matches the value estimated by H12 within a factor of 2 (their Eq. (1)). A crucial aspect of the present approach is

that this external field is assumed to be anisotropic, that is, it does not impinge into the LE clumps on the back side (in the direction of the observer). As a result, the external field contributes to the H$_2$O excitation without generating absorption in the pumping far-IR lines (though some absorption is nevertheless produced by the internal field). As shown in Fig. A.2a, the LE component is expected to dominate the emission of the submm lines 2−6, as well as the emission of the majority of the far-IR lines. The required mass of the LE component is 3.5×10^7 $M_{\odot}$, consistent with the mass inferred from the CO lines for the CND (S12), and the IR luminosity is 2.6×10^{10} $L_{\odot}$.

A key assumption of the present model is that the external radiation field does not produce absorption in the far-IR lines, as otherwise (that is, in a perfectly isotropic radiation field) the strengths of the far-IR lines would weaken, and in particular, the H$_2$O $2_{21}-1_{10}$ line at 108 μm line would be predicted to be observed in absorption. The proposed anisotropy could be associated with the heating by the central AGN, and it seems possible as long as the source is optically thin in the far-IR. Radiative transfer in 3D would be required to check this feature. On the other hand, the external field, while having an important effect on the far-IR lines, has a secondary effect on the submm lines, which are primarily pumped by the internal (isotropic) radiation field (that is, by the dust that is mixed with H$_2$O). With the caveat of the assumed intrinsic radiation anisotropy in mind, we preliminary favor this model over the pure collisional one in predicting the H$_2$O submm fluxes and conclude that radiative pumping most likely plays an important role in exciting the H$_2$O in the CND of NGC 1068.

From the models for these two very different sources and the case of Mrk 231 studied previously (G-A10), we conclude that the excitation of the submm H$_2$O lines other than the $1_{11}-0_{00}$ one is dominated by radiative pumping, though the relatively low-lying $2_{02}-1_{11}$ line may still have a significant "collisional" contribution in some very warm/dense nuclear regions, and the radiative pumping may be enhanced with collisional excitation of the low-lying 1_{11} and 2_{12} levels. These individual cases also show that composite models to account for the full H$_2$O far-IR/submm spectrum in a given source may be a rather general requirement.